



Assessment of the ethanol oxidation activity and durability of Pt catalysts with or without a carbon support using Electrochemical Impedance Spectroscopy



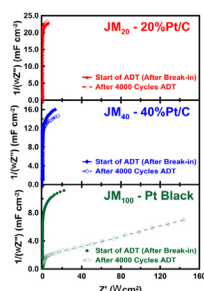
Farhana S. Saleh, E. Bradley Easton*

Faculty of Science, University of Ontario Institute of Technology, 2000 Simcoe Street North, Oshawa, Ontario, Canada L1H 7K4

HIGHLIGHTS

- The durability of JM catalysts with different wt% Pt were studied using EIS.
- The ethanol oxidation activity of these catalysts was also evaluated.
- JM₂₀ catalyst had highest durability and ethanol oxidation performance.
- JM₂₀ and JM₄₀ showed no carbon corrosion after potential cycling, just Pt growth.
- EIS showed JM₁₀₀ (Pt-black) had increased $R_{\text{electronic}}$ after potential cycling.

GRAPHICAL ABSTRACT



ARTICLE INFO

Article history:

Received 29 March 2013

Received in revised form

26 July 2013

Accepted 29 July 2013

Available online 6 August 2013

Keywords:

Durability protocol

EIS

Degradation

Catalyst layer

PEM fuel cell

EOR

ABSTRACT

We compared the stability and performance of 3 commercially available Johnson Matthey catalysts with various Pt loadings (20, 40 and 100%) using two different accelerated durability testing (ADT) protocols. The various Pt-loaded catalysts were tested by means of a series of intermittent life tests (1, 200, 400, 1000, 2000, 3000 and 4000 cycles). The electrochemical surface area (ECSA) loss of electrode was investigated by electrochemical technique (CV). The use of EIS as an accelerated-testing protocol distinctly elucidates the extent of degradation of Johnson Matthey catalysts with various Pt loading. Using EIS, it was possible to show that Pt-black catalyst layers suffer from increased electronic resistance over the course of ADT which is not observed when a corrosion stable carbon support is present. The effect of Pt loading was further elucidated by comparing the electrocatalytic activity of the catalyst layers towards ethanol oxidation reaction (EOR). The catalyst layer with the lowest Pt loading showed the enhanced EOR performance.

© 2013 Elsevier B.V. All rights reserved.

1. Introduction

In response to the energy needs of modern society and emerging ecological concerns, the pursuit of novel, low-cost, and environmentally friendly energy conversion and storage systems has raised significant interest. Among various energy conversion

* Corresponding author.

E-mail address: brad.easton@uoit.ca (E.B. Easton).

transportation applications [8–11]. Both academia and the fuel cell industry are actively working to gain understanding of the failure mechanisms of fuel cell systems. Among other fuel cell components, the degradation of electrocatalyst layer is often found to be a significant cause of cell death [12,13]. Electrocatalysts have large role to both high cost and insufficient durability in today's PEM fuel cell technology, hindering its commercialization [14–18]. Durability study will allow developing electrocatalysts that can make fuel cells more stable, longer lasting, and more resistant to carbon monoxide poisoning. Thus, economic viability of cost-competitive fuel cells depends notably on understanding and improving the durability and the reliability of the CLs.

To meet the automotive targets of activity and durability for PEM fuel cells, the electrocatalyst needs to have a durable support material and active catalyst. Platinum (Pt) supported on high surface area carbon substrates is still the most widely used electrocatalysts in low temperature PEM fuel cells [19–23]. The carbon support enables uniform dispersion of Pt nanoparticles, in addition to providing electronic continuity. During normal automotive operation, PEM fuel cell catalysts undergo thousands of cycles including start-stop and load or potential cycles. Degradation caused by this cycling can be evaluated as a loss of electrochemical surface area (ECSA) [24]. Pt dissolution plays an important role in the ECSA loss [25–27]. It can occur as a result of both potential cycling and carbon corrosion [28–35]. The corrosion of the electrocatalyst support is an additional issue with durability [16,36,37]. Also, high potential significantly accelerates corrosion of carbon [38–41]. The electrochemical corrosion of carbon support results in decreased ECSA due to the loss of electronic conductivity and electrical isolation of the catalyst particles. Presence of Pt particles has also been suspected to speed up carbon corrosion [17,42]. The loss of Pt ECSA over time, because of corrosion of the carbon support and Pt dissolution/aggregation/Oswald ripening, is considered one of the major contributors to the degradation of fuel cell performance [27,43,44].

Potential cycling is a widely used way to test the stability and durability of fuel cell catalysts [35,45,46]. Catalyst degradation due to potential cycling has been investigated extensively in the literature [30,47,48]. Knowledge of these mechanisms has been used to develop accelerated durability testing (ADT) for rapid characterization of catalyst durability under cyclic potentials. The need for ADTs is apparent given the target lives for fuel cell systems: 5000 h for automotive, and 40,000 h for stationary systems [8,43,49]. These tests are also crucial to developers in order to quantitatively evaluate the trade-offs in cost (e.g. lower platinum group metal [PGM] loading), lifetime (e.g. a lower surface area carbon with better corrosion resistance) and performance (e.g. thinner membrane or a gas diffusion layer with better water management properties). The stringent requirements on durability evaluation have led to the development of accelerated testing protocols for PEM fuel cells. However, these protocols focus on one degradation mechanism and they seem less suited to study degradation and its effects on processes in the CL. Since this layer contains supported catalyst as well as ionomer phase, several mechanisms act concurrently. We have worked to define the degradation mechanisms, and understand these mechanisms to allow the design of improved fuel cell materials and components. We have reported on the development of the appropriate accelerated-testing protocols for a quick and uniform screening of entire CL components (Pt dissolution/agglomeration, carbon support corrosion, ionomer degradation) [50]. The degradation of catalysts includes the two aspects of catalytic metals and carbon support, which influence each other. Previously, we described how EIS can clearly diagnose the corrosion of carbon support under accelerated condition. Here, we have advanced our study of EIS in

degradation analysis by studying a case where the Pt loading is different, which leads to a different level of interaction between Pt and the carbon support. EIS was used here for the first time to clarify the dominant degradation processes that occur when the metal loading is varied, as well as illustrating the importance of a stable carbon support.

The scope of this paper is to evaluate the effect of Pt loadings on catalyst durability using our developed ADT protocols. Cyclic voltammetry (CV) was used to monitor the changes in the effective ECSA. Electrochemical impedance spectroscopy (EIS) measurements were made at the start, middle and end of the tests to help understand the modes of electrocatalyst layer degradation. End-of-period diagnosis is carried out after each aging period, including CV and EIS. A combination of such degradation measurements with CV and EIS adds valuable information about the underlying cause of the change in catalyst performance and also allows mechanistic insights on the degradation process. Thus, our strategy for ex-situ testing of fuel cell CL degradation combines the determination of the ECSA loss and/or the change in activity with CV and EIS. This document describes EIS protocol to successfully assess the performance and durability of 3 different Pt-loaded catalysts (20, 40 and 100%) from Johnson Matthey.

2. Experimental

2.1. Electrode preparation

Pt-based catalysts of various Pt loading (20, 40 and 100%) were purchased from Johnson Matthey, and are hereafter referred to as JM₂₀ (HiSPEC 3000), JM₄₀ (HiSPEC 4000) and JM₁₀₀ (HiSPEC 1000), respectively. Both Pt/CB systems have same carbon. A thin film of catalyst, coated on a glassy carbon (GC) was applied to examine the activity and durability of catalysts. Catalyst inks were prepared by dispersing 10 mg of the catalysts powder with a 50:50 mixture of isopropyl alcohol and water (400 μ L) followed by 100 μ L Nafion solution to give a total volume of 500 μ L. The mixture was ultrasonicated for approximately 60 min to achieve a uniform suspension.

A 2 μ L droplet of the well-dispersed catalyst ink was deposited onto the clean, polished, glassy carbon electrode (diam. = 3 mm, CH instruments) using a micro syringe such that it covers the entire surface of glassy carbon. The ink droplet was allowed to dry for 30 min in air at room temperature prior to durability testing. The Pt loading of 0.11 mg cm⁻², 0.22 mg cm⁻², and 0.56 mg cm⁻² were used for JM₂₀, JM₄₀, and JM₁₀₀, respectively.

2.2. Physical characterization

Transmission Electron Microscopy (TEM) images were acquired using a Philips CM 10 instrument equipped with an AMT digital camera system. The catalysts powders were dispersed in ultrapure water and applied to nickel 400 mesh formvar coated carbon reinforced grids and allowed to dry under air. Grids were then scanned in a Philips CM 10 TEM at 100 kV.

Thermogravimetric analysis (TGA) of the catalyst materials was conducted using a TA Instruments Q600 SDT thermal analyzer. Samples were heated from room temperature to 1000 °C at a heating rate of 20 °C min⁻¹ under flowing air (20 mL min⁻¹) on a SDT Q 600 instrument.

2.3. Electrochemical measurements

2.3.1. Electrochemical cell

A single compartment glass cell was used for the electrochemical measurements. A GC disk electrode (0.071 cm²) coated

with electrocatalyst acted as the working electrode (WE). High surface area Pt wire was applied as a counter electrode (CE), and an Ag/AgCl electrode was used as the reference electrode (RE). Sulfuric acid (H_2SO_4 , 0.5 M) was employed as the electrolyte. All electrochemical measurements were performed using a Solatron 1470E Multichannel Potentiostat and a Solartron 1260 frequency response analyzer controlled using Multistat software (Scribner Associates).

2.3.2. Activity measurements

Cyclic voltammetry (CV) and linear sweep voltammetry (LSV) responses were measured under a saturated N_2 atmosphere in the presence of sulfuric acid solution and a mixture of ethanol and sulfuric acid solution, respectively. The WE was first conditioned by cycling at 50 mV s^{-1} for 20 cycles, and then was scanned at 20 mV s^{-1} for 2 cycles over a range of $-0.25 \sim 1.1 \text{ V}$ vs Ag/AgCl. A steady-state voltammogram of the second scan that defined the beginning-of-life (BOL) was recorded to calculate the electrochemical surface area (ECSA) ($\text{m}^2 \text{ g}_{\text{Pt}}^{-1}$) of Pt in the catalyst. ECSA was calculated by

$$\text{ECSA} = Q_{\text{Pt}} / \{(210 \mu\text{C cm}^{-2}_{\text{Pt}})(\text{Pt loading})\} \quad (1)$$

where $210 \mu\text{C cm}^{-2}_{\text{Pt}}$ is the average value for reduction of 1 monolayer of H^+ on Pt. Charge for reduction and adsorption of a monolayer of H^+ on Pt, Q_{Pt} (C cm^{-2}), was calculated by subtracting the double layer charge from the total charge in hydrogen adsorption areas of the CV, which was generally between 0.05 V and 0.4 V.

The electrocatalytic activity of the catalysts toward ethanol oxidation was measured and LSVs were obtained in 0.5 M sulfuric acid and 0.5 M sulfuric acid + 1.0 M ethanol solution. The electrolyte solutions were prepared by diluting sulfuric acid (Fisher Scientific) and ethanol (95%, Commercial Alcohols Inc.). All solutions were purged by bubbling N_2 for at least 10 min.

2.3.3. Durability measurements

2.3.3.1. Aging mode. A standard CV protocol was used to subject the cells to accelerated durability testing (ADT) with triangle sweep cycles between -0.25 V and 1.1 V at 50 mV s^{-1} scan rate. The cells were aged for up to 4000 cycles in 0.5 M H_2SO_4 solution.

2.3.3.2. End-of-period diagnosis. The same end-of-period diagnosis procedures were executed for all three catalysts. The effect of aging on cell performance was monitored by measuring the ECSA. Cyclic voltammetry at 20 mV s^{-1} scan rate was used to measure the ECSA at beginning of tests (BOT), during the tests (after 200, 400, 1000, 2000 and 3000 cycles) and at the end-of-tests (EOT) (after 4000 cycles). The impedance data were collected followed by CV at BOT, during the tests and at EOT to determine the effect of aging on the high frequency resistance, and to analyze the sources of cell voltage loss. All impedance spectra were obtained over 100 kHz to 0.1 Hz frequency range at a DC bias potential of 0.2 V vs Ag/AgCl. The uncompensated resistance was subtracted from all impedance spectra.

For each catalyst, a minimum of 3 catalyst layer were prepared and subjected to ADT, enabling the estimation of measurement error. A high degree of reproducibility was achieved; error bars and standard deviation are shown in tables and figures where appropriate.

3. Results

3.1. Evaluation of Pt catalyst durability with CV protocol

To investigate the electrochemical durability of the Pt catalyst layers, accelerated durability testing (ADT) was conducted in a

H_2SO_4 solution (0.5 M) as the electrolyte solution to mimic the environment of the electrode membrane interface in PEM fuel cell. Under this specific condition, the deterioration of a catalyst was accelerated. To test the durability of Pt catalysts, we used a protocol similar to that proposed previously [50]. The effect of aging on the electrocatalytic activity of the modified electrodes was examined by cycling the electrode potential several times with the appropriate lower (-0.25 V vs. Ag/AgCl) and upper (1.1 V vs. Ag/AgCl) potential limits at a scanning rate of 50 mV s^{-1} for 4000 cycles in a nitrogen saturated atmosphere and recording the corresponding CV in the same solution. The typical CVs for all the three catalysts were recorded before, during and after 4000 potential cycles. Fig. 1 shows the CVs of the JM₂₀, JM₄₀ and JM₁₀₀ modified electrodes after aging for 200, 400, 1000, 2000, 3000, and 4000 potential scans. Fine structures of hydrogen absorption/desorption peaks are clearly appeared in these figures. A reduction peak centered at 0.80 V can be observed during the negative going potential sweep. This reduction peak can be attributed to the reduction of platinum oxide. The feature of the curve is in good agreement with the literature [51].

The ECSA provides important information regarding the number of available active sites. The ECSA accounts not only for the catalyst surface available for charge transfer but also includes the access of a conductive path to transfer the electrons to and from the electrode surface. Hydrogen adsorption/desorption in an electrochemical set up is commonly used to evaluate the ECSA. Since ECSA is a critical factor in analyzing the catalytic activity of electrodes, the changes in ECSA for each catalyst during the durability test were measured. It can be seen from Fig. 1 that a reduction of the hydrogen adsorption and desorption in the CVs appeared on all catalysts with the potential cycling, which shows a decrease of the ECSA. ECSA of the catalyst was estimated from the coulombic charge for the hydrogen desorption (QH) in the cyclic voltammograms as discussed before (Experimental section).

After 200 cycles, the Pt oxide reduction peak (for JM₂₀ and JM₄₀ catalysts) appeared as a shoulder but further increase in the number of cycles (1000) resulted in a clearly distinguished second peak in addition to the Pt oxide reduction peak. This observation is in agreement with the studies in the literature where these peaks are attributed to oxidation and reduction reactions of surface oxygen groups attached to carbon [30]. As the number of cycles increased, the intensity of the peaks corresponding to carbon oxidation/reduction also increased. There was a positive shift of the platinum oxide reduction peaks during the potential cycling which can be attributed to the change in the surface composition of the electrocatalysts.

The initial Pt surface areas before the oxidation treatments were examined by CV, and the measured Pt surface areas are 41.5 and $29.0 \text{ m}^2 \text{ g}_{\text{Pt}}^{-1}$ for JM₂₀ and JM₄₀, respectively. Note that these values are in the reasonable range as reported by others [52,53]. The surface area difference between the two catalysts may necessarily be due to the Pt dispersion as well as Pt particle size difference. In fact, if one examines carefully at the TEM images and the corresponding particle size distribution histograms (Fig. 2), it can be seen that the Pt size on JM₂₀ is slightly smaller than that on JM₄₀. The JM₂₀ catalyst shows spherical Pt nanoparticles with a relatively narrow size distribution uniformly distributed in high dispersion on the carbon black. Agglomeration of the particles appears to be scarce. On the other hand, for the JM₄₀ catalyst (Fig. 2(b)), a higher amount of decoration with metallic nanoparticles is observed than in the case of the JM₂₀. Moreover, the particle distribution is not homogeneous for all support grains, and, in contrast to the JM₂₀, the platinum particles tend to agglomerate (also apparent from Fig. 2(b)). JM₄₀ catalyst with a higher metal loading shows a broader size distribution centered at about 4.44 nm compared to

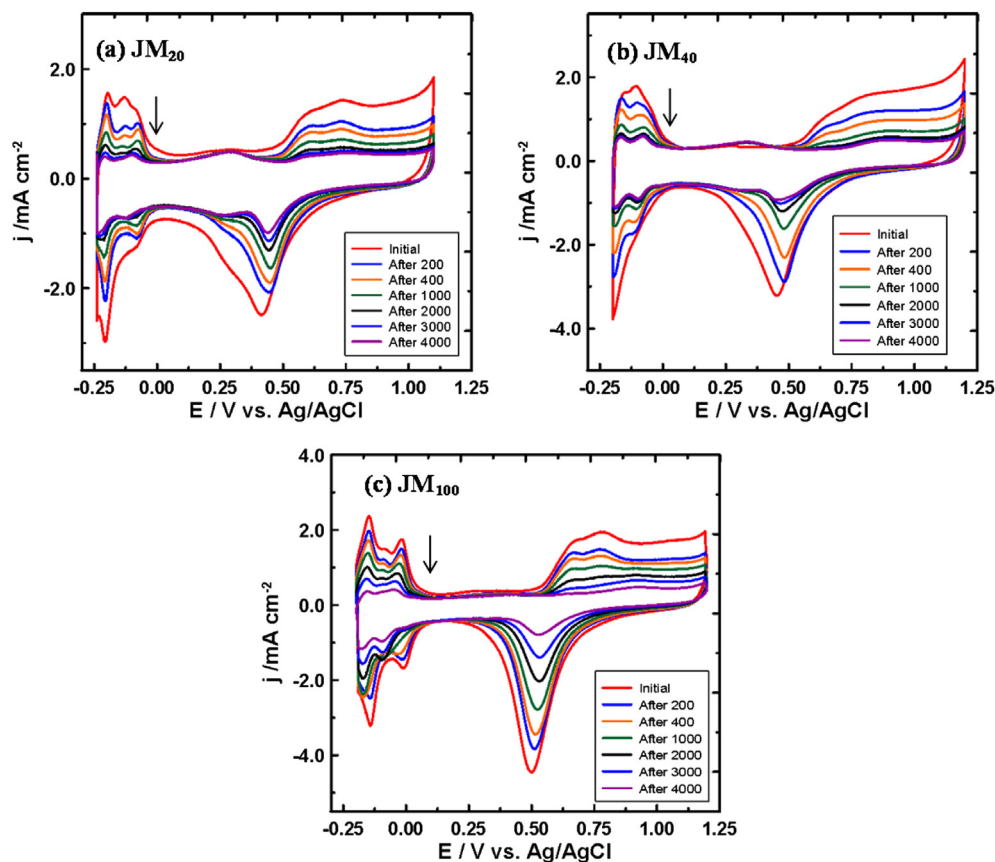


Fig. 1. CVs of (a) JM₂₀, (b) JM₄₀, and (c) JM₁₀₀ before and after the repeated potential cycling in N₂-purged 0.5 M H₂SO₄ at a scan rate of 20 mV s⁻¹.

that of lower Pt-loaded JM₂₀ catalyst at about 3.02 nm. Thus, the high initial ECSA of JM₂₀ is attributed to the smaller particle size of Pt nanoparticles loaded on the CB support. The initial ethanol oxidation reaction (EOR) activity of JM₂₀ catalyst is also higher than that of JM₄₀. The electrocatalytic activities of JM₂₀, JM₄₀ and JM₁₀₀ for EOR were investigated and Fig. 3 shows the corresponding LSV curves in N₂-saturated 1.0 M C₂H₅OH + 0.5 M H₂SO₄ solution at 20 mV s⁻¹ vs Ag/AgCl. The onset potential of EOR for the JM₂₀ is 89 and 155 mV lower than those of JM₄₀ and JM₁₀₀, respectively. The mass activity of Pt electrocatalysts for ethanol oxidation is a critical parameter regarding the practical application of Pt electrocatalysts. The peak currents of the JM₂₀, JM₄₀ and JM₁₀₀ are 429.0 A g⁻¹_{Pt}, 169.0 A g⁻¹_{Pt} and 55.0 A g⁻¹_{Pt}, respectively. It is clear that the catalytic activity of JM₂₀ is 2.5 times and 7.8 times higher than that of JM₄₀ and JM₁₀₀, respectively. This noticeably indicates that the utilization of the Pt metal by the JM₂₀ is much higher than that of the JM₄₀ and JM₁₀₀ catalysts.

The loss of the ECSA of the Pt catalyst with the cycling number is plotted in Fig. 4(a). The results show that the initial ECSA of JM₂₀ before potential cycling test is higher than that of JM₄₀ and JM₁₀₀. Furthermore, it can be seen that the ECSA of the Pt catalysts decreases with the increase of the number of cycles. It is believed that the surface area loss shown in Fig. 4(a) largely result from Pt dissolution and Pt aggregation. In addition, the rate of surface loss in the first 400 cycles is quite similar in every catalyst. We propose that the rapid surface area loss of Pt nanoparticles upon initial cycling largely results from rapid dissolution of small Pt nanoparticles into the acid solution. After 4000 cycles, the ECSA decreased from 41.6 to 13.7 m² g⁻¹ for JM₂₀ from 29.0 to 10.7 m² g⁻¹ for JM₄₀, and from 10.8 to 1.7 m² g⁻¹ for JM₁₀₀. Furthermore, most of

the ECSA loss for the case of JM₂₀ and JM₄₀ occurs within 1000 cycles and then the degradation becomes very small. On the contrary, the ECSA loss of the JM₁₀₀ catalyst which has the highest Pt loading continues to decline linearly during the whole ADT process. According to Fig. 4(b), JM₂₀ and JM₄₀ catalysts showed a higher percentage of ECSA at EOL, i.e. 33% and 34.5%, respectively compared to that of JM₁₀₀ catalyst (16%). These data demonstrate that the JM₂₀ and JM₄₀ catalysts are much more stable than the JM₁₀₀ catalyst.

The effect of Pt loading on the double layer region of supported and non-supported Pt catalysts was also investigated and compared in Fig. 4(c). As can be seen from Fig. 4(c), a decrease in the double layer capacitance of the electro catalysts was observed with increasing platinum loading. The principle of double layer capacitance at the electrode/electrolyte interface is the accumulation of the electric charges on the electrode surface while ions of opposite charge are arranged in the electrolyte side. Double layer capacitance depends critically on surface area of carbon material used in electrodes. The higher the specific surface area of the carbon the higher the specific capacitance of the catalyst is obtained. In addition, carbon materials with larger pores should be capable of delivering high power because it can be discharged/charged at higher current density because larger pores would provide more favorable and quicker pathway for ions to penetrate [54]. Since JM₂₀ has the highest specific surface area because of the lowest Pt loading (Fig. not shown) and the lowest average particle size with 3.02 nm, its capacitance is the highest one when compared to other electro catalysts (average particle size of JM₄₀ is 4.44 nm). At the same time, JM₁₀₀ exhibited the lowest double layer capacitance which has the largest particle size of 6.0 nm and lowest specific

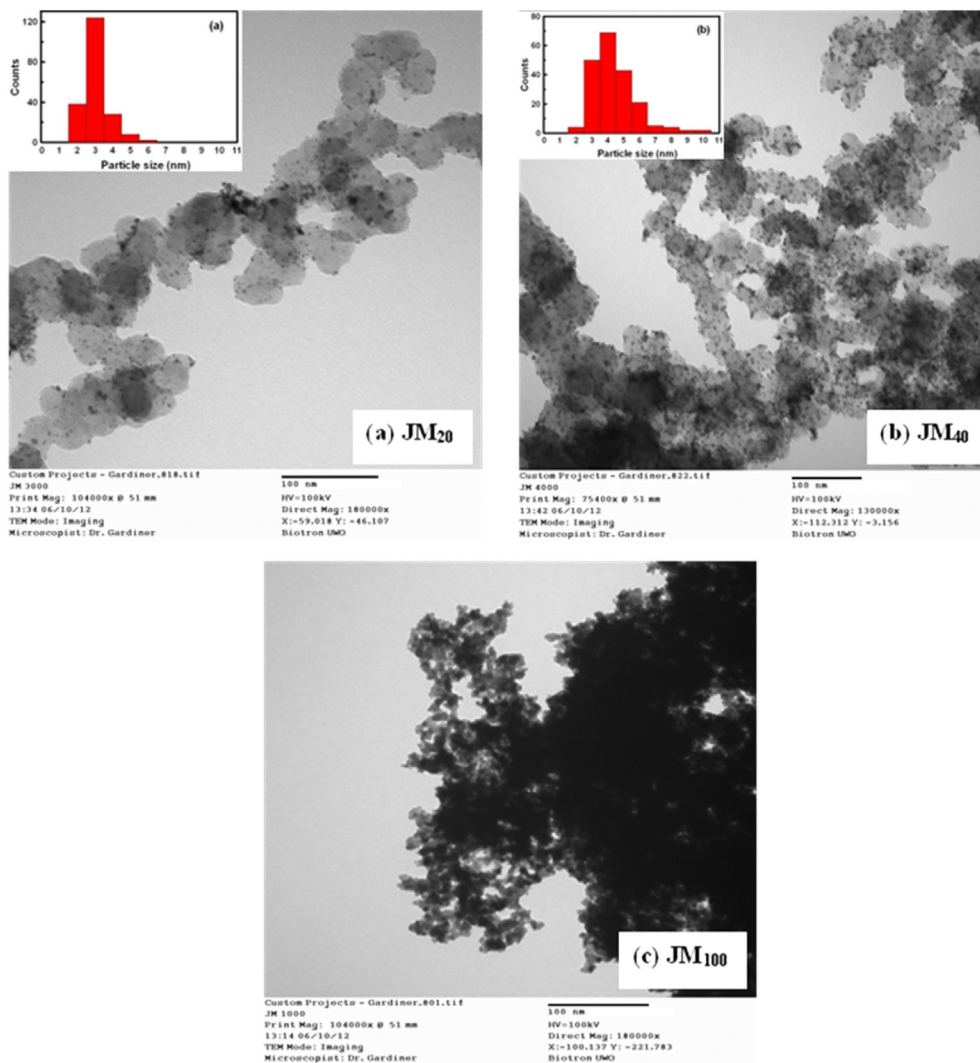


Fig. 2. TEM images of different catalyst layers. (a) JM₂₀, and (b) JM₄₀, and (c) JM₁₀₀. Inset shows the corresponding size distribution of Pt nanoparticles on CB.

surface area. A summary of electrochemical properties of JM₂₀, JM₄₀, and JM₁₀₀ electrocatalysts layer before and after ADT can be found in Table 1.

To distinctly elucidate difference in the degradation between various Pt-loaded catalysts, all these catalysts were further diagnosed by EIS after the consecutive CV cycle tests.

3.2. Evaluation of Pt catalyst durability with EIS protocol

Electrochemical impedance spectra of the JM₂₀, JM₄₀ and JM₁₀₀ catalyst modified electrodes in the 0.5 M H₂SO₄ aqueous electrolyte solution acquired at 0.2 V vs. Ag/AgCl are reported in Figs. 5–7. Nyquist plots illustrate the total resistance present in the electrode

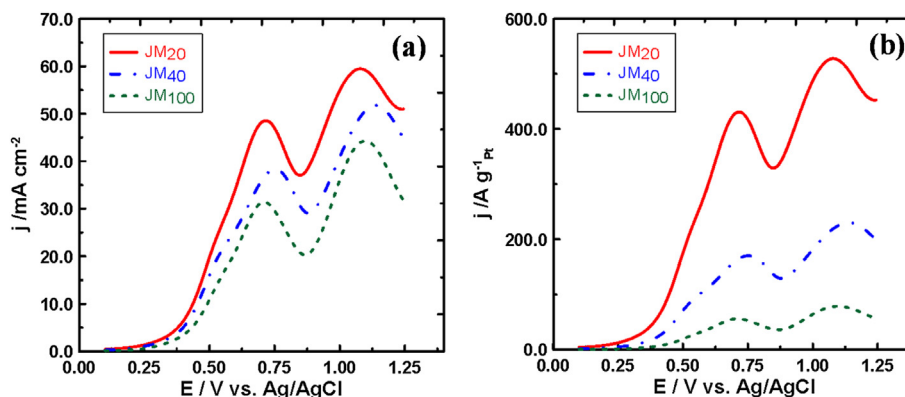


Fig. 3. CVs for ethanol oxidation reaction in 1 M EOH + 0.5 M H₂SO₄ at JM₂₀, JM₄₀, and JM₁₀₀ catalyst modified electrodes. Potential scan rate: 20 mV s⁻¹. The current normalized on the basis of (a) geometric area, and (b) Pt loading.

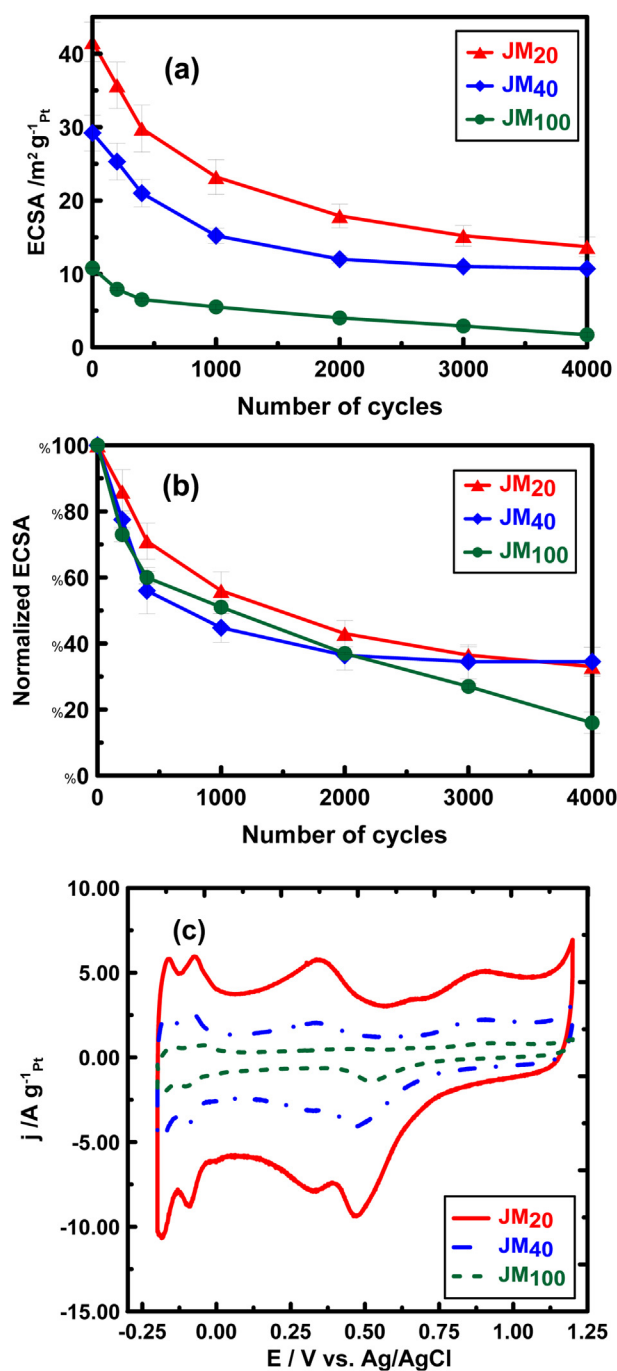


Fig. 4. (a) Change of ECSAs for JM₂₀, JM₄₀, and JM₁₀₀ electrocatalysts during the repeated potential cycling. (b) Comparison of loss of ECSAs for JM₂₀, JM₄₀, and JM₁₀₀ electrocatalysts as a function of the number of CV cycles. (c) Comparison of CVs of JM₂₀, JM₄₀, and JM₁₀₀ at the end-of-tests (EOT).

Table 1

Summary of the electrochemical properties of the JM₂₀, JM₄₀, and JM₁₀₀ electrocatalysts.

Catalyst	ECSA _{Pt} ($\text{m}^2 \text{g}^{-1}$)		Average Pt particle size (nm)	EOR activity	
	BOL	EOL		Anodic current density ($\text{A g}^{-1} \text{Pt}$)	Onset potential (mV)
JM ₂₀	41.6 ± 2.67	13.7 ± 1.34	1.9	429.0	245
JM ₄₀	29.0 ± 2.45	10.7 ± 0.10	2.9	169.0	334
JM ₁₀₀	10.8 ± 0.05	1.7 ± 0.33	6.0	55.0	400

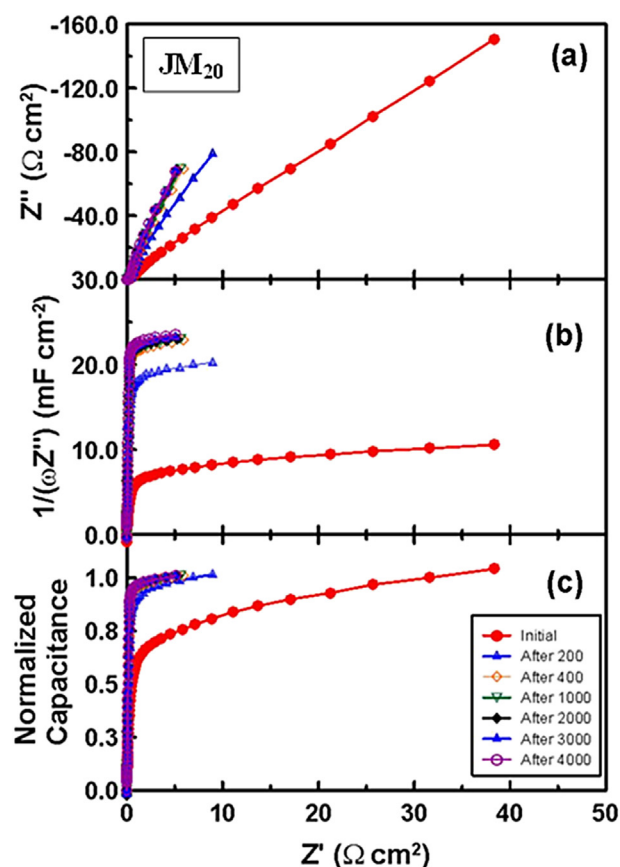


Fig. 5. EIS responses obtained at a DC bias potential of 0.2 V vs. Ag/AgCl for the JM₂₀ catalyst layer after various CV cycles plotted as (a) Nyquist plots and (b) capacitance plots and (c) normalized capacitance plots.

material. The Nyquist plot consists of (1) a high-frequency intercept on the real Z' axis, and (2) a straight line at the very low-frequency region. For JM₂₀, in the Nyquist plot (Fig. 5(a)) at high frequency, a Warburg-like response (45° slope) is observed, which corresponds to ion/electron migration through the catalyst layer. Normally, it is safe to assume that this results from ionic resistance in the catalysts layer. At low frequency, the impedance plot curves up to a limiting capacitance response (vertical) which corresponds to the total capacitance of the catalyst layer. With JM₂₀ modified electrode, the internal resistance decreased with increasing potential cycling, mainly due to the increasing hydration of the catalyst layer, leading to a decrease in ionic resistance. We can see a very little change in resistance as well as capacitance after this hydration “break-in” (from 400 cycles to 4000 cycles). This can be better visualized through capacitance plots (Fig. 5(b)). Using capacitance plots, both the conductivity within the catalyst layer as well as the active area can be simultaneously visualized. The steepness of the initial slope of the capacitance plot is indicative of the conductivity within the catalyst layer and the limiting capacitance is proportional to active surface area (Pt + C) [55,56]. Thus, a higher limiting capacitance normally means that a larger fraction of the CL is being utilized. We can see similar steepness of the slopes (Warburg lengths) throughout the cycling process, which means that there is no drastic change in carbon surface occurred due to cycling and only decay process here, is Pt area loss. During the potential cycling, the capacitance initially increases until it reaches a maximum value, as more of the active area of the electrode is accessed and remains unchanged up to 4000 cycles. Incomplete wetting of Nafion ionomer at initial stage may be an issue for this increase in capacitive value that resisted proper proton conduction through the layer.

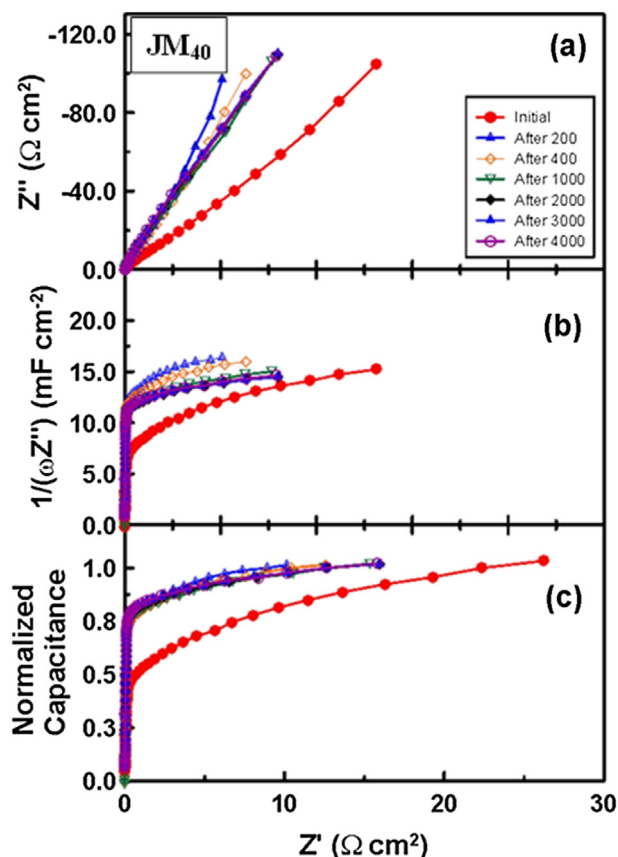


Fig. 6. EIS responses obtained at a DC bias potential of 0.2 V vs. Ag/AgCl for the JM₄₀ catalyst layer after selective CV cycles plotted as (a) Nyquist plots and (b) capacitance plots and (c) normalized capacitance plots.

Fig. 6 shows the impedance responses of JM₄₀ as a function of cycle number. Impedance signatures of the JM₄₀ are similar to that acquired for JM₂₀. The Nyquist plots are similar to those obtained for the JM₂₀ layers (Fig. 5) with the notable exception that after 200 cycles a slight increase in the resistivity is seen. This suggests that the higher loading of Pt resulted in relatively lower degradation resistance. No massive change in capacitance was evident after 2000 cycles. Capacitance plots are shown in Fig. 6(b) that better show how conductivity varies across the layer. It should be noted that some of the observed difference in capacitance between these two electrodes may be due to differing relative contributions from the Pt and C surfaces, or the relative continuations of double layer and Faradaic capacitances.

The impedance results of JM₁₀₀ without any carbon content shows a gradual increase in resistivity or decrease in conductivity which is in contrast to either of the carbon-supported Pt catalysts. These results are shown in Fig. 7. Impedance spectra taken at consecutive potential cycling show an increase in the electrode resistance at the high-frequency intercepts of the x-axis, an increase in the catalyst layer resistance, leading to a change in the shape of the curves. Change in the low-frequency region could reflect changes in the pore structure of the catalyst layer.

Fig. 8(a) shows an example of the Nyquist plot obtained with each electrode type at the end-of-life (EOL) with various Pt loading. From these we can see that the conductivity decreases with the increase of Pt loading. There appears to be a higher resistance for electrodes containing 100% Pt after the potential cycling test. This may be in part to due to the absence of a stable carbon support that allows another degradation pathway to become significant for

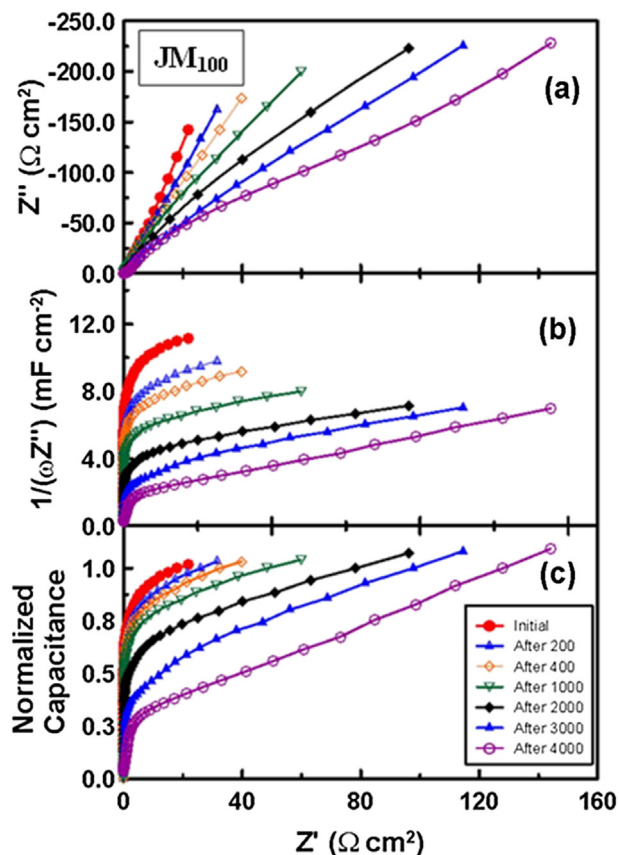


Fig. 7. EIS responses obtained at a DC bias potential of 0.2 V vs. Ag/AgCl for the JM₁₀₀ catalyst layer after selective CV cycles plotted as (a) Nyquist plots and (b) capacitance plots and (c) normalized capacitance plots.

JM₁₀₀ that was not present in both JM₂₀ and JM₄₀. Both Pt dissolution and agglomeration occurs for all catalysts under these ADT conditions. Furthermore, we do not expect the catalyst layer ionomer to degrade under these conditions for any of these catalysts. The changes in impedance spectra observed for JM₁₀₀ do appear similar to that observed when the carbon support corrodes [50]. However, since this is Pt black, there is no carbon present to corrode. However, the same effect, an increase in electronic resistance does explain this phenomenon. In addition to increasing the electrode surface area, a stable carbon support provides a conductive electronic pathway to the electrolyte interface, which will be independent of the presence/absence of a metal catalyst. Thus, when a carbon supported is not employed as in the case of Pt black, any irreversible dissolution of Pt will create a gap on the catalyst layer over time, increasing electronic resistivity and eventually creating gaps in catalyst layer in illustrated in Fig. 9. This increase in resistance can only serve to accelerate performance degradation over time and explains why the relative rate of measured ECSA loss was higher for JM₁₀₀ at the later stages of ADT compared to the carbon supported catalysts.

This increase in resistivity can be better seen through capacitance plots. Fig. 8(b) shows capacitance plots obtained for JM₂₀, JM₄₀ and JM₁₀₀ catalyst modified electrodes at EOL. It can be seen that for JM₂₀, the initial slope of the capacitance plot is higher (a steeper slope, shorter Warburg) than that of JM₄₀, indicating that the resistivity is lower in the case of JM₂₀. However, plot obtained for JM₁₀₀ show much lower slopes (longer Warburg), indicating even higher resistivity that arises from conductivity and diffusion limitations. This increasing resistivity is clearly visible in Fig. 8(c),

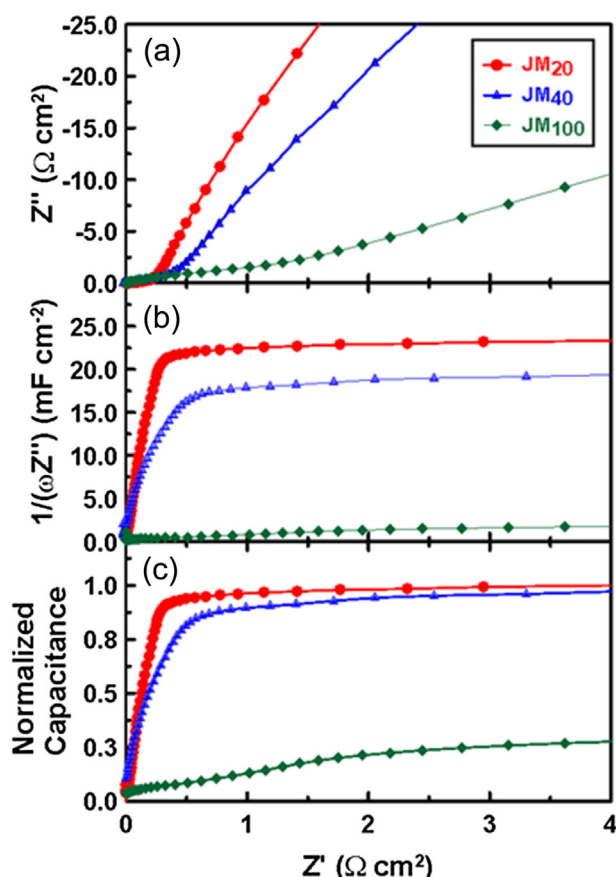


Fig. 8. Comparison of EIS data profiles JM₂₀, JM₄₀, and JM₁₀₀ at the end-of-tests (EOT).

where the capacitances have been normalized by dividing them by the initial capacitance value. Carbon black supported catalyst layers become more and more accessible over time with higher slopes and thus indicating improved ionic resistivity. Incomplete wetting of the catalyst layer at initial stage might be an issue for this increase in capacitance that resists proper proton conduction through the catalyst layer. JM₂₀ catalyst layer also exhibited higher limiting capacitance meaning a higher active area of Pt in JM₂₀ compared to JM₄₀, that agrees well with the CV results and this appears to be responsible for the higher catalytic activity for JM₂₀ towards EOR.

When we compared the specific capacitances (the capacitances have been normalized by dividing them by the mass of carbon) for JM₂₀ and JM₄₀ at the beginning-of-life (BOL), after break-in (BI) and at the end-of-life (EOL) (Fig. 10), we could see that both the catalysts required the break-in period that allowed the catalyst layer to become fully hydrated and for all the catalytic sites to become activated. And after BI, very little change in capacitance can be observed which means no significant corrosion occurred in carbon black support due to accelerated degradation testing. A slight decrease in capacitance after BI for JM₄₀ appears to be due to small degradation of the catalyst layer in the presence of higher loading of Pt.

The specific capacitance comparison at the BOL and EOL for CLs composed of JM₂₀, JM₄₀ and JM₁₀₀ catalysts also confirms the higher long-term stability of JM₂₀ over JM₄₀, and JM₁₀₀. Fig. 11 shows the plots of normalized capacitances at BOL and EOL. It clearly shows that the capacitance plots at EOL for both JM₂₀ and JM₄₀ catalyst layers have increased significantly than those at BOL, while an extensive positive shift including increased resistivity and

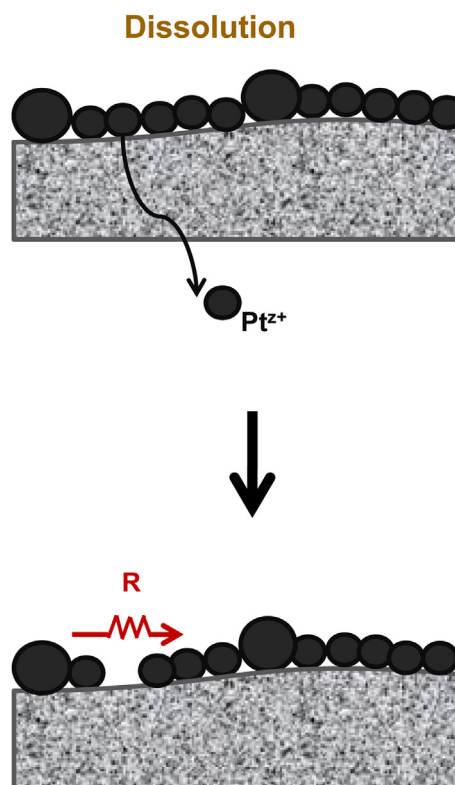


Fig. 9. Schematic representation of the proposed degradation mechanism in JM₁₀₀ catalyst layers.

decreased electronic conductivity is observed for the same measurement for JM₁₀₀ catalyst layer. Thus, JM₂₀ stands out as the highest corrosion resistant catalyst under the same accelerated condition applied.

We have also determined the total catalyst layer resistance, R_{Σ} , for the three Pt based catalysts. A value for R_{Σ} can be determined from a Nyquist plot, by determining the projected length of the Warburg-like component onto the Z' axis, which is defined as $R_{\Sigma}/3$, where R_{Σ} represents the sum of the ionic (R_i) and electronic (R_E) [57,58]. While it is often assumed that for fuel cell electrodes that the electronic contributions to the impedance is negligible and that $R_{\Sigma} = R_i$, we have found that this assumption is not always valid when applied to durability. Fig. 12 shows the plot of R_{Σ} as a function of cycle number obtained with each electrode type. From this we can see there is a slight decrease in R_{Σ} for carbon-supported Pt catalyst layers (JM₂₀ and JM₄₀) that is attributed to decreasing R_i upon hydration, and also confirms that potential cycling does not lead to ionomer degradation under these aging conditions. Furthermore, this also confirms that the carbon support used in JM₂₀ and JM₄₀ is highly stable. However, there appears to be a substantial increase in the total resistance, R_{Σ} , for pure Pt black (JM₁₀₀) when it was cycled from 2000 to 4000. The increase in the impedance of the JM₁₀₀ was attributed to increased electronic resistance upon cycling as discussed previously.

Thus, we can conclude that the impedance data can clarify JM₂₀ to have a higher capacitance than JM₄₀ and JM₁₀₀ catalysts, which show increasing capacitances in the order JM₂₀ > JM₄₀ > JM₁₀₀ (Fig. 8). Since capacitance is related to the active electrochemical area, these results largely support the voltammetric results in Fig. 4(b), where we obtained reasonable values for standard deviation for each catalyst. The JM₂₀ catalyst gives higher capacitances than either the JM₄₀ or JM₁₀₀ catalyst, as expected based on

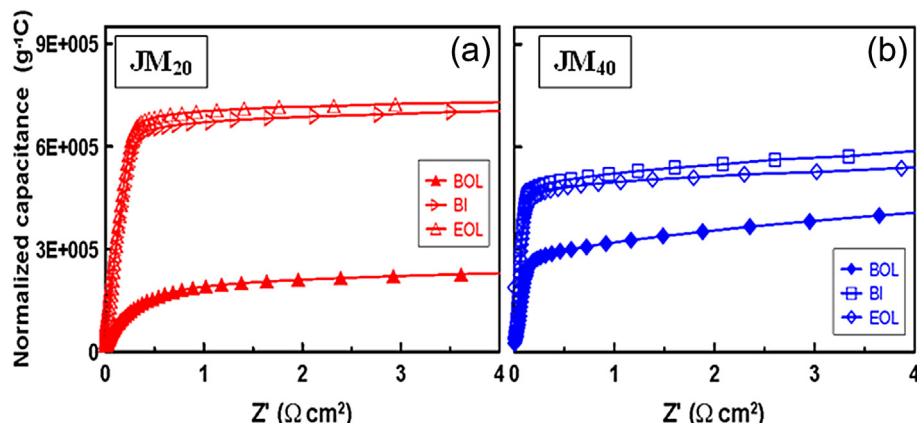


Fig. 10. Comparison of the mass of carbon-normalized capacitances obtained for (a) JM₂₀ and (b) JM₄₀ catalyst layers at the beginning-of-life (BOL), break-in (BI) and at the end-of-life (EOL). Data was acquired at a DC bias potential of 0.2 V vs. Ag/AgCl.

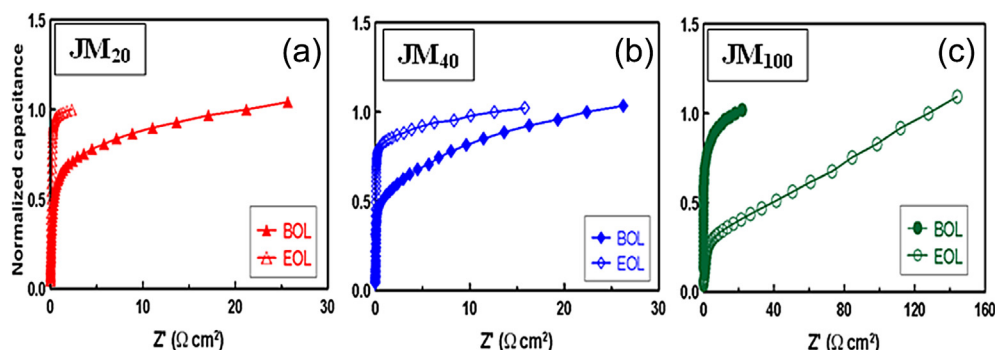


Fig. 11. Comparison of the normalized capacitances obtained for the (a) JM₂₀ catalyst layer with those obtained with (b) JM₄₀, and (c) JM₁₀₀ catalyst layers at the beginning-of-life (BOL) and at the end-of-life (EOL). Data was acquired at a DC bias potential of 0.2 V vs. Ag/AgCl.

voltammetric and ethanol oxidation results (Fig. 3). The lower efficacy of non-supported JM₁₀₀ catalyst relative to carbon black supported ones may arise, at least in part, from significant loss of Pt due to Pt dissolution as well as agglomeration (Fig. 9). Another important factor is the larger Pt particle size, which may reduce the active surface area of the catalyst (Table 1). The resistance profiles shown in Fig. 11 indicate that these differences in active areas are due to differences in the conductivity of the catalyst layer. In other words a larger fraction of the catalyst layer is electrochemically active in electrodes with better and more durable ionic and

electronic conductive pathways. As has already been discussed above, JM₂₀ and JM₄₀ catalysts retain higher ECSA compared to JM₁₀₀ catalyst under the accelerated condition and at 3000 cycles, ECSAs for both JM₂₀ and JM₄₀ were reduced by about 60%, whereas JM₁₀₀ showed more than 70% loss in ECSA. This difference in ECSA can be explained by the involvement of R_E increase for JM₁₀₀ along with Pt particle growth in the degradation process. Fig. 12 supports this assumption where we can observe a 4-fold higher R_Σ value for JM₁₀₀ in comparison to those obtained with JM₂₀ and JM₄₀ catalysts. Each catalyst layer was tested in triplicate and the results for the R_Σ (Fig. 12) seemed to be fairly consistent across each replicates, well within expected tolerances for catalyst layers deposited by this method. Thus, the application of EIS into the ADT protocol reveals that improved utilization of the Pt metal as well as stable carbon support has great impact on the durability of Pt-based catalyst layers.

4. Conclusions

In this work, Pt-based CLs degradation has been compared using a time-effective and reliable EIS method of a series of Johnson Matthey CLs with different amounts of Pt content. Accelerated-testing experiments have been developed and were applied to examine material degradation. The EIS data has the added benefit in that it can be used to study the ionic and electronic conductivity profiles within the catalyst layer. By using EIS with our ADT protocol, a detailed comparison of the durability of Johnson Matthey catalysts with various Pt loading was made. It was clearly demonstrated that Pt-black catalyst layers are prone to increased

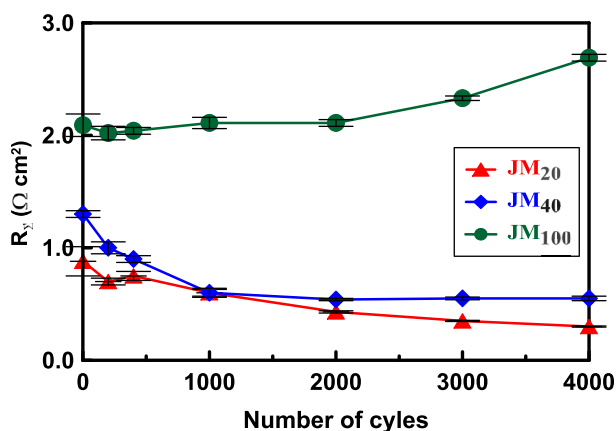


Fig. 12. Variation on the total electrode resistance, R_Σ , with the number of CV cycles for JM₂₀, JM₄₀, and JM₁₀₀ electrocatalysts.

electronic resistance when Pt dissolution/agglomeration occurs. As a result of this second degradation pathway, Pt-black catalysts layer can display a faster rate of performance degradation than carbon supported catalysts. This second contribution could be elucidated from the EIS data but not discernable from CV measurements.

Our results also suggest JM₂₀ has long-term durability as well as promising corrosion resistance superior to 40% and 100% Pt-loaded catalysts. In addition, tests for EOR activity for the studied catalysts shows that a decrease in Pt loading lowers the onset potential for ethanol electro-oxidation and enhances the ethanol oxidation current density. Based on this, we report JM₂₀ to be the most active and most durable/stable over long-term use in CLs.

Acknowledgments

This work was supported by Alcohol Countermeasure Systems Corp., the Natural Sciences and Engineering Research Council (NSERC) of Canada and UOIT. The authors thank Dr. Richard Gardiner (University of Western Ontario) for TEM images.

References

- [1] A. Boudghene Stambouli, E. Traversa, *Renewable Sustainable Energy Rev.* 6 (2002) 433.
- [2] H.A. Gasteiger, S.S. Kocha, B. Sompalli, F.T. Wagner, *Appl. Catal. B Environ.* 56 (2005) 9.
- [3] W. Vielstich, H. Gasteiger, A. Lamm, in: *Handbook of Fuel Cells, Fundamentals, Technology and Applications*, Wiley, West Sussex, 2003.
- [4] J. Wee, K. Lee, S. Kim, *J. Power Sources* 165 (2007) 667.
- [5] H. Liu, C. Song, L. Zhang, J. Zhang, H. Wang, D. Wilkinson, *J. Power Sources* 155 (2006) 95.
- [6] K. Sopian, W.R. Wan Daud, *Renew. Energy* 31 (2006) 719.
- [7] L. Zhang, J. Zhang, D. Wilkinson, H. Wang, *J. Power Sources* 156 (2006) 171.
- [8] A.A. Franco, S. Passot, P. Fugier, C. Anglade, E. Billy, L. Guetaz, N. Guillet, E. De Vito, S. Mailley, *J. Electrochem. Soc.* 156 (2009) B410.
- [9] K.J.J. Mayrhofer, J.C. Meier, S.J. Ashton, G.K.H. Wiberg, F. Kraus, M. Hanzlik, M. Arenz, *Electrochem. Commun.* 10 (2008) 1144.
- [10] J.R. Yu, T. Matsuura, Y. Yoshikawa, M.N. Islam, M. Hori, *Electrochem. Solid-State Lett.* 8 (2005) A156.
- [11] S. Zhang, X.-Z. Yuan, J.N.C. Hin, H. Wang, J. Wu, K.A. Friedrich, M. Schulze, *J. Power Sources* 195 (2010) 1142.
- [12] W. Liu, K. Ruth, G. Rusch, *J. New Mater. Electrochem. Syst.* 4 (2001) 227.
- [13] W. Liu, M. Crum, *ECS Trans.* 3 (2006) 531.
- [14] J. Xie, D. Wood, D. Wayne, T. Zawodzinski, P. Atanassov, R. Borup, *J. Electrochem. Soc.* 152 (2005) A104.
- [15] M. Mathias, H. Gasteiger, R. Makharia, S. Kocha, T. Fuller, J. Pisco, *Abstr. Pap. Am. Chem. Soc.* 228 (2004) U653.
- [16] S.D. Knights, K.M. Colbow, J. St-Pierre, D.P. Wilkinson, *J. Power Sources* 127 (2004) 127.
- [17] D.A. Stevens, J.R. Dahn, *Carbon* 43 (2005) 179.
- [18] A. Taniguchi, T. Akita, K. Yasuda, Y. Miyazaki, *J. Power Sources* 130 (2004) 42.
- [19] N. Yousfi-Steiner, P. Mocoteguy, D. Candusso, *J. Power Sources* 194 (2009) 130.
- [20] B. Wahdame, D. Candusso, X. François, *Int. Hydrogen Energy* 34 (2009) 967.
- [21] T. Matsumoto, T. Komatsu, K. Arai, T. Yamazaki, M. Kijima, H. Shimizu, Y. Takasawa, J. Nakamura, *Chem. Commun.* (2004) 840.
- [22] T.J. Schmidt, U.A. Paulus, H.A. Gasteiger, R.J. Behm, *J. Electroanal. Chem.* 508 (2001) 41.
- [23] C. Bock, C. Paquet, M. Couillard, G.A. Botton, B.R. MacDougall, *J. Am. Chem. Soc.* 126 (2004) 8028.
- [24] J.G. Liu, Z.H. Zhou, X.X. Zhao, Q. Xin, G.Q. Sun, B.L. Yi, *Phys. Chem. Chem. Phys.* 6 (2004) 134.
- [25] R.M. Darling, J.P. Meyers, *J. Electrochem. Soc.* 150 (2003) A1523.
- [26] R.M. Darling, J.P. Meyers, *J. Electrochem. Soc.* 152 (2005) A242.
- [27] P.J. Ferreira, G.J. la O', Y. Shao-Horn, D. Morgan, R. Makharia, S. Kocha, H.A. Gasteiger, *J. Electrochem. Soc.* 152 (2005) A2256.
- [28] X. Wang, W.Z. Li, Z.W. Chen, M. Waje, Y.S. Yan, *J. Power Sources* 158 (2006) 154.
- [29] C.H. Paik, T.D. Jarvi, W.E. O'Grady, *Electrochem. Solid-State Lett.* 7 (2004) A82.
- [30] M. Cai, M.S. Ruthkosky, B. Merzougui, S. Swathirajan, M.P. Balogh, S.H. Oh, *J. Power Sources* 160 (2006) 977.
- [31] K.H. Kangasniemi, D.A. Condit, T.D. Jarvi, *J. Electrochem. Soc.* 151 (2004) E125.
- [32] J.P. Meyers, R.M. Darling, *J. Electrochem. Soc.* 153 (2006) A1432.
- [33] C.A. Reiser, L. Bregoli, T.W. Patterson, J.S. Yi, J.D.L. Yang, M.L. Perry, T.D. Jarvi, *Electrochem. Solid-State Lett.* 8 (2005) A273.
- [34] M. Waje, W.Z. Li, Y.S. Yan, *Electrochem. Soc. Trans.* 3 (2006).
- [35] B. Merzougui, S. Swathirajan, *J. Electrochem. Soc.* 153 (2006) A2220.
- [36] N. Sisofo, 4th Annual Inter. Vancouver, BC, Canada, Fuel Cell Testing Workshop, September 12–13, 2007.
- [37] A. Taniguchi, T. Akita, K. Yasuda, Y. Miyazaki, *J. Power Sources* 130 (2004) 42–49.
- [38] H. Tang, Z. Qi, M. Ramani, J.F. Elter, *J. Power Sources* 158 (2006) 1306.
- [39] T.F. Fuller, G. Gray, *ECS Trans.* 1 (2006) 345.
- [40] H. Chizawa, Y. Ogami, H. Naka, A. Matsunaga, N. Aoki, T. Aoki, *ECS Trans.* 3 (2006) 645.
- [41] P.T. Yu, W. Gu, R. Makharia, F.T. Wagner, H.A. Gasteiger, *ECS Trans.* 3 (2006) 797.
- [42] K. Kinoshita, J. Bett, *Carbon* 12 (1974) 525.
- [43] Y.Y. Shao, G.P. Yin, Y.Z. Gao, *J. Power Sources* 171 (2007) 558.
- [44] Z.M. Peng, H. Yang, *J. Am. Chem. Soc.* 131 (2009) 7542.
- [45] A.S. Arico, A. Stassi, E. Modica, R. Ornelas, I. Gatto, E. Passalacqua, *J. Power Sources* 178 (2008) 525.
- [46] P. Yu, M. Pemberton, P. Plasse, *J. Power Sources* 144 (2005) 11.
- [47] K. Teranishi, K. Kawata, S. Tsushima, S. Hirai, *Electrochem. Solid-State Lett.* 9 (2006) A475.
- [48] H.R. Colon-Mercado, H. Kim, B.N. Popov, *Electrochem. Commun.* 6 (2004) 795.
- [49] X. Yu, S. Ye, *J. Power Sources* 172 (2007) 145.
- [50] F.S. Saleh, E.B. Easton, *J. Electrochem. Soc.* 159 (2012) B546.
- [51] D. He, S. Mu, M. Pan, *Carbon* 49 (2011) 82.
- [52] H.-H. Wang, Z.-Y. Zhou, Q. Yuan, N. Tian, S.-G. Sun, *Chem. Commun.* 47 (2011) 3407.
- [53] G.J.M. Janssen, E.F. Sitters, A. Pfrang, *J. Power Sources* 191 (2009) 501.
- [54] D. Qu, H. Shi, *J. Power Sources* 74 (1998) 99.
- [55] E.B. Easton, P.G. Pickup, *Electrochim. Acta* 50 (2005) 2469.
- [56] N.Y. Jia, R.B. Martin, Z.G. Qi, M.C. Lefebvre, P.G. Pickup, *Electrochim. Acta* 46 (2001) 2863.
- [57] M. Lefebvre, R.B. Martin, P.G. Pickup, *Electrochem. Solid-State Lett.* 2 (1999) 259.
- [58] M. Lefebvre, Z. Qi, D. Rana, P.G. Pickup, *Chem. Mater.* 11 (1999) 262.